A method for establishing a continuous constitutive model of welded metals

L. Xing, M. Zhan, P.F. Gao, F. Ma

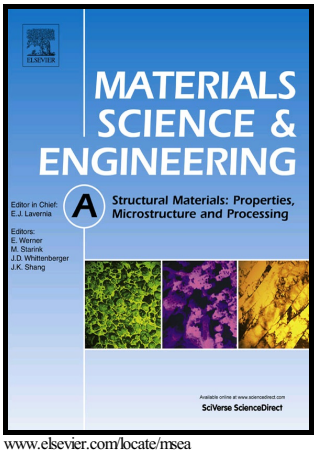

www.elsevier.com/locate/msea

PII: S0921-5093(18)30080-7
DOI: https://doi.org/10.1016/j.msea.2018.01.062
Reference: MSA36016

To appear in: *Materials Science & Engineering A*

Received date: 13 November 2017
Revised date: 15 January 2018
Accepted date: 16 January 2018

Cite this article as: L. Xing, M. Zhan, P.F. Gao and F. Ma, A method for establishing a continuous constitutive model of welded metals, *Materials Science & Engineering A,* https://doi.org/10.1016/j.msea.2018.01.062

A method for establishing a continuous constitutive model of welded metals

L. Xing [a], M. Zhan [a, *], P. F. Gao [a], F. Ma [b]

[a] State Key Laboratory of Solidification Processing, School of Materials Science and Engineering, Northwestern Polytechnical University, Xi'an 710072, China

[b] Long March Machinery Factory, China Aerospace Science and Technology Corporation, Chengdu, 610100, China

[*] Corresponding Author. Tel.: +86-29-88460212-801; Fax: +86-029-88495632; Email: zhanmei@nwpu.edu.cn (M. Zhan)

Abstract

Developing an accurate and continuous constitutive model across the weld bead and heat affected zone (HAZ) is an urgent challenge to address the inhomogeneous property distribution and its effects on plastic deformation of welded metals. In this study, such a universal method was proposed, in which the continuous variation in flow stress across these zones was characterized via the relationship among the flow stress, microhardness and weld shape. Through the method, the continuous constitutive model of welded metals can be expressed as a function of weld shape. Essentially, this continuous constitutive model eliminates the dependence of the accuracy on the partition of HAZ in the discrete constitutive model. Using the method, continuous constitutive models of a 2219 aluminum alloy welded plate (AAWP) and a QSTE340 welded tube (WT) were set up. These constitutive models were applied to the finite element (FE) modelings of longitudinal and transverse tensions of the 2219 AAWP and bending of the QSTE340 WT, respectively. The comparisons from simulation and experiment of both of the tensions show that the continuous constitutive model can accurately describe the deformation responses of the welded metals in simple loading processes. Comparison in prediction results of welded tube bending based on the continuous and discrete constitutive models shows that the continuous one presents higher prediction precision in complicated plastic deformation processes. Finally, the transverse tensile deformation behavior of the 2219 AAWP was obtained using the continuous constitutive model.

Keywords: Weld bead; HAZ; Continuous constitutive model; Microhardness; Application.

1. Introduction

In recent years, all kinds of parts made of welded metals through plastic forming processes obtain wider application in the aircraft and automotive industries, because of the manufacturing advantages of low cost, short production period and great variety [1-4]. However, the plastic forming abilities of welded metals dependent on inhomogeneous material properties in the weld (including the weld bead and heat affected zone (HAZ)) and parent metal. At present, the research about the influence of the inhomogeneous material properties on the plastic forming abilities of welded metals was widely carried out, and the most commonly used method is finite element simulation (FES). One of the key problems of FES is how to make the calculation accuracy sufficiently high, so as to obtain reliable results. For this purpose, it is necessary to obtain more accurate constitutive model of the weld [5].

Many researches [6-8] showed that there are obvious differences in the material properties of the weld bead and HAZ, and the material properties vary continuously within these zones. The accuracy of the FES is closely related to the degree that how the constitutive model of the weld can adequately describe these differences and variations of the material properties. According to the treatment for the differences, the constitutive models established by the existing methods for the weld are divided into two categories, i.e., the homogeneous one and the heterogeneous one.

1.1. Homogeneous constitutive model

The homogeneous constitutive model ignores the differences in material properties of the weld bead and HAZ in the weld, i.e., the weld is considered as uniform material. Cheng [9] adopted the uniaxial tension tests of “weld-only” specimens to obtain a homogeneous constitutive model of the weld of the stainless-steel tailor-welded blank (TWB). Saunders [10] and Abdullah [11] determined the homogeneous constitutive models of the weld of steel TWBs based on the mixing rule for analyzing the influence of the size of the tensile specimen and studying the formability of the TWBs. The homogeneous constitutive model describes the material properties of the weld in welded metals roughly, and it is applicable in some cases without too high accuracy requirements.

1.2. Heterogeneous constitutive model

The heterogeneous constitutive model considers the differences in material properties of the weld bead and HAZ. According to the treatment for the variations of the material properties within these two zones, the heterogeneous constitutive model can be divided into the average one, the discrete one and the continuous one.

1.2.1 Average heterogeneous constitutive model

The average heterogeneous constitutive model ignores the variations of the material properties within the weld bead and HAZ, that is, the materials of these two zones are considered uniform, respectively. Lee [12] obtained the respective constitutive models of the weld bead and the HAZ of TWBs based on the mixing rule. Reis [13] and Roque [14] obtained the respective mechanical properties of the weld bead and HAZ of low-carbon steel welded plates and welded tubes through the empirical formula of microhardness. Li [15] determined the average heterogeneous constitutive models of dual-phase high-strength steel welded plates using the 3D digital image correlation technique. The constitutive models obtained in the above studies describe the average material properties of the weld bead and HAZ, respectively, ignoring the variations of the material properties within these zones.

1.2.2 Discrete heterogeneous constitutive model

The discrete heterogeneous constitutive model considers the variations of the material properties within the weld bead and HAZ, by subdividing these two zones, respectively. Zhan [16] established the discrete constitutive models of the weld bead and HAZ based on the mixed material tensile experiment and microhardness test. By dividing the HAZ, this method received the material properties of the divided regions. In the process, the variations of the material properties within the HAZ were characterized, however, the continuity of the variations was ignored. It has a certain gap with reality and will affect the calculation accuracy of FES [17-20].

1.2.3 Continuous heterogeneous constitutive model

The continuous heterogeneous constitutive model not only considers the variations of the material properties within the weld bead and HAZ, but also considers the continuity of the variations. Song [21] determined a constitutive model of the weld of the laser TWB by establishing the relationships between the strength coefficient, the hardening exponent and the distance to the center of the weld based on the nanoindentation test. This constitutive model takes into account the differences and the variations of the material properties in the weld. However, this method has certain requirement for the ratio of hardness to initial yield strength of material within 0.5 and 3. Meanwhile, a reference strain needs to be determined in this method, thus the method has a dependence on the reference strain. These would limit its universal applicability. Therefore, it is urgent to find a new and universal method for establishing a continuous constitutive model of welded metals.

In this study, such a method was proposed. By obtaining the continuously varying flow stress in the weld, the dependence of the method on the material is eliminated, and a universal method is achieved. Section 2 describes the method in details by taking the welded tube as an example. Applications of the proposed method are given

in Section 3 by applying it to a 2219 aluminum alloy welded plate (AAWP) and a QSTE340 welded tube (WT).

2. Proposal of the method

This study proposed a universal method for establishing the continuous constitutive model of welded metals. In this method, according to the static equilibrium and the integral principle, a mechanical model considering the continuous variation of flow stress was established. Meanwhile, the continuous variation of flow stress was characterized via the relationship among the flow stress, microhardness and weld shape.

The welded metals mainly include welded plate and welded tube. Thus, in order to facilitate elaboration, this section takes the welded tube as an example to describe the detailed establishment process of the continuous constitutive model.

2.1. Establishment of mechanical model

To establish the mechanical model considering the continuous variation of flow stress, a mixed material specimen under the longitudinal tension was adopted in this study, in which the weld bead, HAZ and parent metal are included, as shown in Fig. 1. Meanwhile, this study employed the most widely used equal strain rule, which is based on the assumption that the distribution of the axial strain is uniform on the cross section, that is, the axial strain of weld bead, HAZ, parent metal and the average axial strain of the mixed material (ε_w, ε_h, ε_p and ε_m) in tensile specimen are equal [11, 16] (Eq. (1)).

$$\varepsilon_w = \varepsilon_h = \varepsilon_p = \varepsilon_m \tag{1}$$

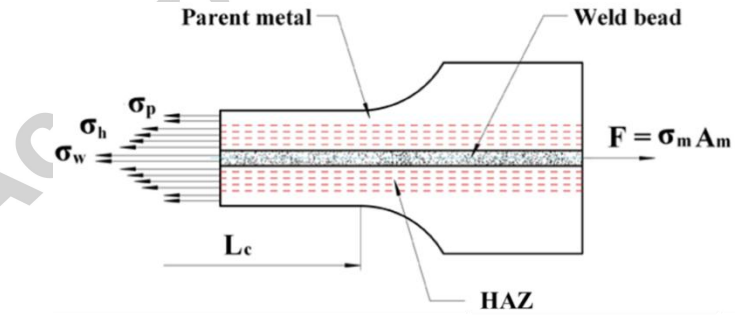

Fig. 1. The model of the mixed material specimen.

According to the static equilibrium, Eq. (2) can be obtained.

$$\sigma_w A_w + \sigma_h A_h + \sigma_p A_p = \sigma_m A_m \tag{2}$$

where A_w, A_h, A_p and A_m denote the cross sectional area of the weld bead, HAZ, parent metal and mixed material specimen, respectively; σ_w, σ_h, σ_p and σ_m are the flow stress

of the weld bead, HAZ, parent metal and mixed material specimen, respectively.

The continuous variations of the flow stress within the weld bead and HAZ were taken into account in Eq. (2). The shape of the weld in the welded tube was approximately arc shape (Fig. 2). In order to describe the characteristics of the continuous variations of flow stress, Eq. (2) can be converted to Eq. (3) according to the integral principle.

$$\int_{\alpha_{wl}}^{\alpha_{wr}} \sigma_w G d\alpha + \int_{\alpha_{wr}}^{\alpha_{hr}} \sigma_h G d\alpha + \int_{\alpha_{hl}}^{\alpha_{wl}} \sigma_h G d\alpha + \int_{\alpha_{hr}}^{\alpha_{mr}} \sigma_p G d\alpha + \int_{\alpha_{ml}}^{\alpha_{hl}} \sigma_p G d\alpha = \int_{\alpha_{ml}}^{\alpha_{mr}} \sigma_m G d\alpha \qquad (3)$$

where $G = \frac{1}{2}\left[(r+t)^2 - r^2\right]$; r and t are the inner radius and the thickness of the welded tube, respectively; α_{wl} and α_{wr} denote the central angle at the left and right interfaces between the weld bead and HAZ, respectively; α_{hl} and α_{hr} denote the central angle at the left and right interfaces between the HAZ and parent metal, respectively; α_{ml} and α_{mr} denote the central angle at the left and right edges of the mixed material specimen, respectively, as shown in Fig. 2.

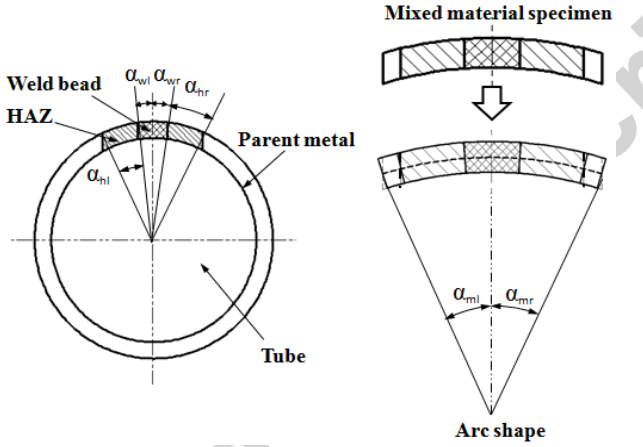

Fig. 2. Cross sections of welded tube and mixed material specimen.

2.2. Characterization of continuous variation of flow stress

The continuous variation of flow stress was characterized via the relationship among the flow stress, microhardness and weld shape. Many studies have shown that the ratio of the microhardness to flow stress is approximately constant [14,16,20]. That is to say, the flow stresses of the weld bead and HAZ are proportional to the microhardnesses, as shown in Eq. (4).

$$\sigma_w = \sigma_p \frac{HV_w}{HV_P} \quad \text{or} \quad \sigma_h = \sigma_p \frac{HV_h}{HV_P} \qquad (4)$$

where HV_w, HV_h and HV_p denote the Vickers microhardness of the weld bead, HAZ and parent metal, respectively.

Therefore relative to the parent metal, the ratios of the flow stress's increment to microhardness's increment in the HAZ and weld bead are equal (Eq. (5)):

$$\frac{\sigma_h - \sigma_p}{HV_h - HV_p} = \frac{\sigma_w - \sigma_p}{HV_w - HV_p} \tag{5}$$

Eq. (5) can be converted to Eq. (6):

$$\sigma_h = \sigma_p + \frac{HV_h - HV_p}{HV_w - HV_p}(\sigma_w - \sigma_p) \tag{6}$$

According to Eq. (6), the continuous variation law of flow stress in HAZ can be determined via establishing the continuous variation law of microhardness.

Variation laws of microhardness are different for different welded joints due to the differences in welding material and the experienced temperature cycling. Generally, the material in the weld suffers high temperature and stays at high temperature for a short time, the microstructure in the zone will occur dynamic recrystallization and the microhardness and strength will increase [22]. Furthermore, the closer to the center of the weld, the greater the probability of dynamic recrystallization occurs. Hence the microhardness from the weld bead to the parent metal shows a downward trend. This tendency can be described by many decay functions, such as exponential decay function, sigmoidal function and so on. For ease of deduction, this study adopted a typical decay function, the exponential decay function, to describe this variation law. Considering that the width of the weld bead is small and the microhardness in the zone varies little, the microhardness of the weld bead is assumed to be uniform, and it was represented using HV_w. Meanwhile, in some welding processes, such as friction stir welding (FSW), there exist an advancing side and a retreating side near the weld bead, and the material properties on these two sides are asymmetric [23]. Therefore, the microhardness of the HAZ on both sides of the weld bead was described by different formulas, respectively, as shown in Eq. (7).

$$\begin{cases} HV_{hr} = HV_w - (HV_w - HV_p)(1 - e^{-\xi_1 \alpha}), & \alpha_{wr} \le \alpha \le \alpha_{hr} \\ HV_{hl} = HV_w - (HV_w - HV_p)(1 - e^{-\xi_2 \alpha}), & \alpha_{hl} \le \alpha \le \alpha_{wl} \end{cases} \tag{7}$$

where HV_{hr} and HV_{hl} denote the microhardness of the HAZ on the right and left sides of the weld bead, respectively; ξ_1 and ξ_2 are the coefficients.

By substituting Eq. (7) into Eq. (6), the continuously varying flow stress within the HAZ can be obtained as Eq. (8).

$$\begin{cases} \sigma_{hr} = \sigma_w - (\sigma_w - \sigma_p)(1 - e^{-\xi_1 \alpha}), & \alpha_{wr} \le \alpha \le \alpha_{hr} \\ \sigma_{hl} = \sigma_w - (\sigma_w - \sigma_p)(1 - e^{-\xi_2 \alpha}), & \alpha_{hl} \le \alpha \le \alpha_{wl} \end{cases} \tag{8}$$

where σ_{hr} and σ_{hl} denote the flow stress of the HAZ on the right and left sides of the weld bead, respectively.

2.3. Establishment of continuous constitutive model

Applying Eq. (8) to Eq. (3), Eq. (9) can be obtained.

$$\int_{\alpha_{wl}}^{\alpha_{wr}} \sigma_w G d\alpha + \int_{\alpha_{wr}}^{\alpha_{hr}} \left[\sigma_w - (\sigma_w - \sigma_p)(1-e^{-\xi_1 \alpha})\right] G d\alpha + \int_{\alpha_{hl}}^{\alpha_{wl}} \left[\sigma_w - (\sigma_w - \sigma_p)(1-e^{-\xi_2 \alpha})\right] G d\alpha + \int_{\alpha_{hr}}^{\alpha_{mr}} \sigma_p G d\alpha + \int_{\alpha_{ml}}^{\alpha_{hl}} \sigma_p G d\alpha = \int_{\alpha_{ml}}^{\alpha_{mr}} \sigma_m G d\alpha \tag{9}$$

By simplifying Eq. (9), the flow stress of the weld bead can be obtained as Eq. (10).

$$\sigma_w = \frac{\sigma_m(\alpha_{mr} - \alpha_{ml}) - \sigma_p\left[\alpha_{mr} + \alpha_{wl} - \alpha_{ml} - \alpha_{wr} + \frac{1}{\xi_1}(e^{-\xi_1 \alpha_{hr}} - e^{-\xi_1 \alpha_{wr}}) + \frac{1}{\xi_2}(e^{-\xi_2 \alpha_{wl}} - e^{-\xi_2 \alpha_{hl}})\right]}{\alpha_{wr} - \alpha_{wl} - \frac{1}{\xi_1}(e^{-\xi_1 \alpha_{hr}} - e^{-\xi_1 \alpha_{wr}}) - \frac{1}{\xi_2}(e^{-\xi_2 \alpha_{wl}} - e^{-\xi_2 \alpha_{hl}})} \tag{10}$$

Making $M_1 = \frac{1}{\xi_1}(e^{-\xi_1 \alpha_{hr}} - e^{-\xi_1 \alpha_{wr}})$ and $M_2 = \frac{1}{\xi_2}(e^{-\xi_2 \alpha_{wl}} - e^{-\xi_2 \alpha_{hl}})$, Eq. (10) can be rewritten as Eq. (11).

$$\sigma_w = \frac{\sigma_m(\alpha_{mr} - \alpha_{ml}) - \sigma_p(\alpha_{mr} + \alpha_{wl} - \alpha_{ml} - \alpha_{wr} + M_1 + M_2)}{\alpha_{wr} - \alpha_{wl} - M_1 - M_2} \tag{11}$$

In summary, the continuous flow stresses of the weld bead and HAZ in welded tube are shown in Eq. (12).

$$\begin{cases} \sigma_w = \dfrac{\sigma_m(\alpha_{mr} - \alpha_{ml}) - \sigma_p(\alpha_{mr} + \alpha_{wl} - \alpha_{ml} - \alpha_{wr} + M_1 + M_2)}{\alpha_{wr} - \alpha_{wl} - M_1 - M_2}, & \alpha_{wl} \le \alpha \le \alpha_{wr} \\ \sigma_{hr} = \sigma_w - (\sigma_w - \sigma_p)(1-e^{-\xi_1 \alpha}), & \alpha_{wr} \le \alpha \le \alpha_{hr} \\ \sigma_{hl} = \sigma_w - (\sigma_w - \sigma_p)(1-e^{-\xi_2 \alpha}), & \alpha_{hl} \le \alpha \le \alpha_{wl} \end{cases} \tag{12}$$

The constitutive models satisfied by the different welded metals are different. Therefore, this study adopted the general formulas Eqs. (13) and (14) to denote the constitutive models of the parent metal and the mixed material of the welded tube, respectively.

$$\sigma_p = f(\varepsilon) \tag{13}$$

$$\sigma_m = g(\varepsilon) \tag{14}$$

Applying Eqs. (13) and (14) to Eq. (12), the continuous constitutive model of the welded tube Eq. (15) can be obtained.

$$\begin{cases} \sigma_w = \dfrac{g(\varepsilon)(\alpha_{mr} - \alpha_{ml}) - f(\varepsilon)(\alpha_{mr} + \alpha_{wl} - \alpha_{ml} - \alpha_{wr} + M_1 + M_2)}{\alpha_{wr} - \alpha_{wl} - M_1 - M_2}, & \alpha_{wl} \le \alpha \le \alpha_{wr} \\ \sigma_{hr} = \sigma_w - \left[\sigma_w - f(\varepsilon)\right](1-e^{-\xi_1 \alpha}), & \alpha_{wr} \le \alpha \le \alpha_{hr} \\ \sigma_{hl} = \sigma_w - \left[\sigma_w - f(\varepsilon)\right](1-e^{-\xi_2 \alpha}), & \alpha_{hl} \le \alpha \le \alpha_{wl} \end{cases} \tag{15}$$

When using the proposed method to establish the continuous constitutive model of a welded plate, the detailed deduction process is similar to that in the above welded

tube, except that the center angles α_{wl}, α_{wr}, α_{hl}, α_{hr}, α_{ml} and α_{mr} are necessary to be replaced by the distances to the center of the weld x_{wl}, x_{wr}, x_{hl}, x_{hr}, x_{ml} and x_{mr} (Fig. 3), respectively. Thus for simplification, here only gives the final continuous constitutive model of the welded plate, as shown in Eq. (16).

$$\begin{cases} \sigma_w = \dfrac{g(\varepsilon)(x_{mr}-x_{ml}) - f(\varepsilon)(x_{mr}+x_{wl}-x_{ml}-x_{wr}+M_1'+M_2')}{x_{wr}-x_{wl}-M_1'-M_2'}, & x_{wl} \le x \le x_{wr} \\ \sigma_{hr} = \sigma_w - [\sigma_w - f(\varepsilon)](1-e^{-\xi_1' x}), & x_{wr} \le x \le x_{hr} \\ \sigma_{hl} = \sigma_w - [\sigma_w - f(\varepsilon)](1-e^{-\xi_2' x}), & x_{hl} \le x \le x_{wl} \end{cases} \quad (16)$$

where $M_1' = \dfrac{1}{\xi_1'}(e^{-\xi_1' x_{hr}} - e^{-\xi_1' x_{wr}})$ and $M_2' = \dfrac{1}{\xi_2'}(e^{-\xi_2' x_{wl}} - e^{-\xi_2' x_{hl}})$; ξ_1' and ξ_2' are the coefficients.

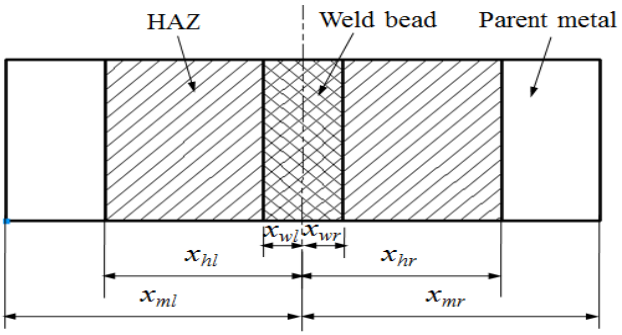

Fig. 3. Cross section of mixed material specimen of welded plate.

The constitutive models established above can accurately describe the continuous variation of the material properties in the weld. Meanwhile, the above proposed method has no dependence on the material, with good universality.

2.4. Implementation procedure

The implementation procedure of the proposed method for determining the continuous constitutive model of welded metals is shown in Fig. 4.

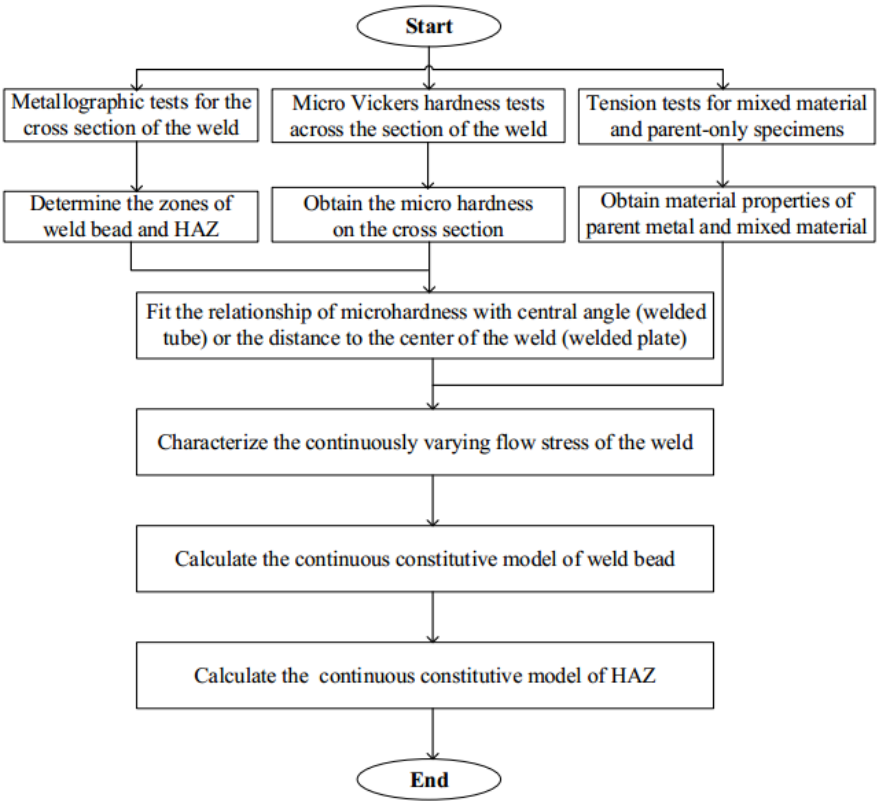

Fig. 4. Flow chart of developing the continuous constitutive model of welded metals.

3. Application of the method

First, using the proposed method, the continuous constitutive models of the 2219 AAWP and the QSTE340 WT were set up. Then, to evaluate the accuracies of the above constitutive models, they were applied to the FE modelings of the simple loading processes (including both longitudinal and transverse uniaxial tensions) and complicated plastic forming process of bending, respectively. Their accuracies were verified by comparing the simulation with the experiment results in load-displacement curve of longitudinal tension and the maximum major strain distribution of transverse tension and by comparing the prediction results of welded tube bending using the continuous and discrete constitutive models, respectively. Meanwhile, the deformation behavior of transverse tension of 2219 AAWP was analyzed.

3.1. Establishment of the continuous constitutive models of the 2219 AAWP and the QSTE340 WT

3.1.1 The continuous constitutive model of the 2219 AAWP

The 2219 AAWP used for this study was manufactured by FSW, and the thickness was 6 mm.

3.1.1.1. Determination of variation law of the microhardness

Fig. 5(a) shows the cross-section of the 2219 FSW joint. According to the shape of the weld, the cross section of welded joint was divided into an upper zone and a lower zone along the thickness direction (Y direction) as shown in Fig. 5 (b).

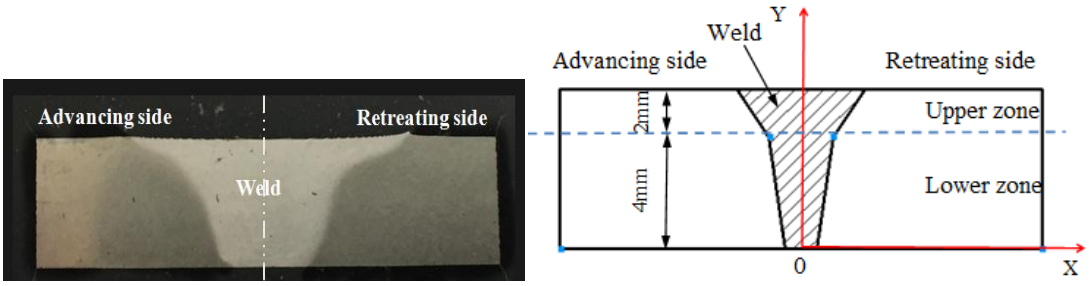

(a) (b)

Fig. 5. The cross-section (a) and partition sketch (b) of the 2219 FSW joint.

The microhardness distributions in the lower zone are shown in Fig. 6. As can be seen from Fig. 6 (a), the variation trends of the microhardness along the X direction under different thicknesses are similar. The microhardnesses in the advancing and retreating sides both firstly decline rapidly and then decrease slowly from the weld bead to the parent metal. These variation trends can be described by the exponential decay function. In order to simplify the calculation, the microhardness distributions of the advancing and retreating sides on the neutral layer of the lower zone were fitted by the exponential decay function (Eq. (7)). The fitting results are shown in Fig. 6 (b), Eqs. (17) and (18), with the fitting precisions R of 0.97 and 0.96 for the advancing and retreating sides, respectively.

$$HV_{hla} = 48.11 + 19.34e^{0.59x} \tag{17}$$

$$HV_{hlr} = 48.11 + 19.34e^{-0.39x} \tag{18}$$

where HV_{hla} and HV_{hlr} denote the microhardness of the HAZ on the advancing and retreating sides in the lower zone, respectively.

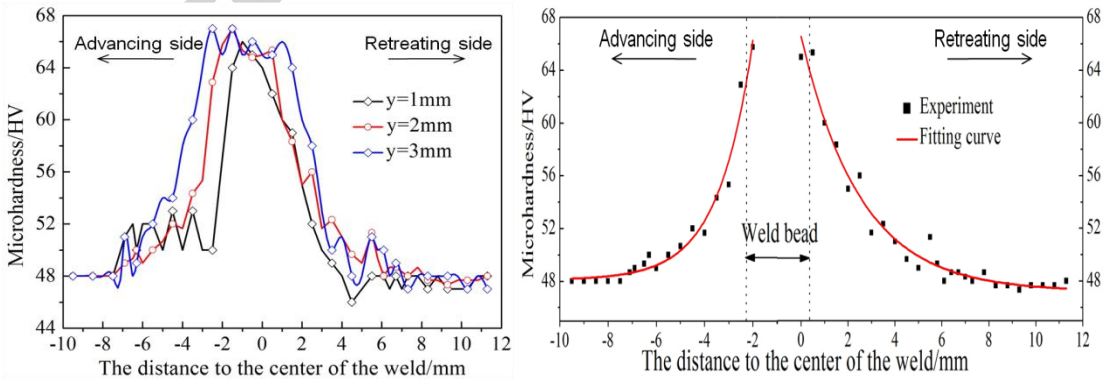

(a) (b)

Fig. 6. Microhardness distributions (a) and fitting curves (b) in the lower zone.

The microhardness distributions in the upper zone are shown in Fig. 7. As can be seen from Fig. 7(a), the variation trends of the microhardness along the X direction under different thicknesses are similar. It can also be seen from Fig. 7(a) that the variation trends of the microhardness along the X direction in the advancing and retreating sides are different. The microhardness in the advancing side first declines rapidly and then decreases slowly from the weld bead to the parent metal, and the variation trend is similar to that in the lower zone. While the microhardness in the retreating side first drops rapidly to a platform and then decreases slowly, and the variation trend can be described by the sigmoidal function (Eq. (19)). According to the above analysis, the microhardnesses in the advancing and retreating sides on the neutral layer of zone were fitted by Eqs. (7) and (19), respectively. The fitting results are shown in Fig. 7 (b), Eqs. (20) and (21), with the fitting precisions R of 0.96 and 0.97, respectively.

$$HV_h = HV_p + \frac{HV' - HV_p}{1 + 10^{(m-x)\cdot g}} \tag{19}$$

where m and g are the coefficients.

$$HV_{hua} = 46.59 + 304.60e^{0.53x} \tag{20}$$

$$HV_{hur} = 46.59 + \frac{11.60}{1 + 10^{0.25x - 1.32}} \tag{21}$$

where HV_{hua} and HV_{hur} denote the microhardness of the HAZ on the advancing and retreating sides in the upper zone, respectively.

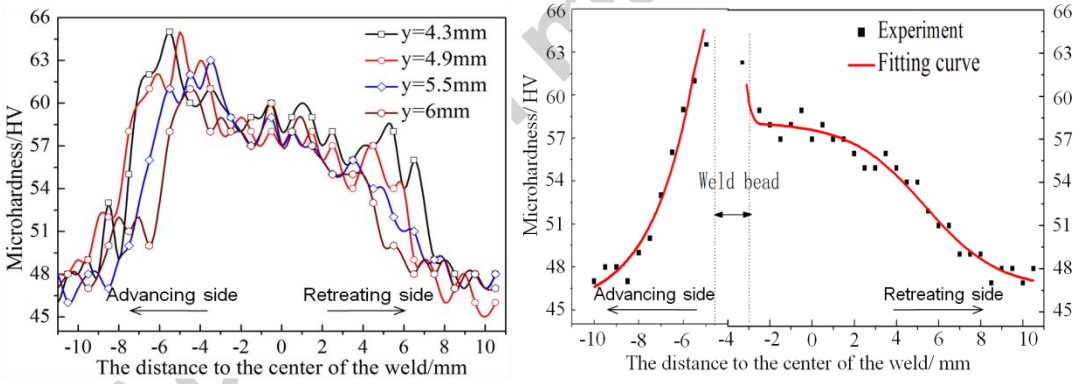

(a) (b)

Fig. 7. Microhardness distributions (a) and fitting curves (b) in the upper zone.

3.1.1.2. Determination of widths of the weld bead and HAZ

The microstructures of the parent metal, HAZ and weld bead of the 2219 AAWP are shown in Fig. 8. As seen from the Fig. 8(a), the parent material is distributed with the uniform strip of grain. The grains of HAZ grow slightly compared with those of the parent metal (Fig. 8(b)). There are small and uniform grains in the weld bead (Fig. 8(c)). By analyzing the microstructure image and the microhardness distribution, the widths of the weld bead in the lower zone (b_{wl}) and upper zone (b_{wu}) were determined

as b_{wl} = 3.0 mm and b_{wu} = 1.5 mm, respectively. The widths of HAZ in the lower zone on the advancing and retreating sides are 4.5 mm and 5.5 mm, respectively. In the upper zone they are 3.5 mm and 5.0 mm, respectively.

3.1.1.3. Determination of stress-strain curves of parent metal and mixed material

The nominal stress-strain and true stress-strain curves of parent metal and mixed material specimens measured by uniaxial tension test are shown in Fig. 9. As seen from the Fig. 9(a), the yield stress and elongation of the mixed material are higher than those of the parent metal, especially the elongation, with an increment of 8.24%. By fitting the true stress-strain curves of the parent metal and the mixed material specimen, it is found that the fitting degrees of Swift equation Eq. (22) [24] are higher. Therefore, the constitutive models of the parent metal and the mixed material specimen expressed by the equation are shown Eqs. (23) and (24), with the fitting precisions R of 0.98 and 0.97, respectively.

$$\sigma = K(\varepsilon + \varepsilon_0)^n \quad (22)$$

where K is the strength coefficient; n is the hardening exponent; ε_0 is the pre-strain value. This equation considers the effect of pre-strain due to blank manufacturing by roll forming and welding.

$$\sigma_p = 255.051(\varepsilon + 0.000258)^{0.170} \quad (23)$$

$$\sigma_m = 296.718(\varepsilon + 0.00196)^{0.204} \quad (24)$$

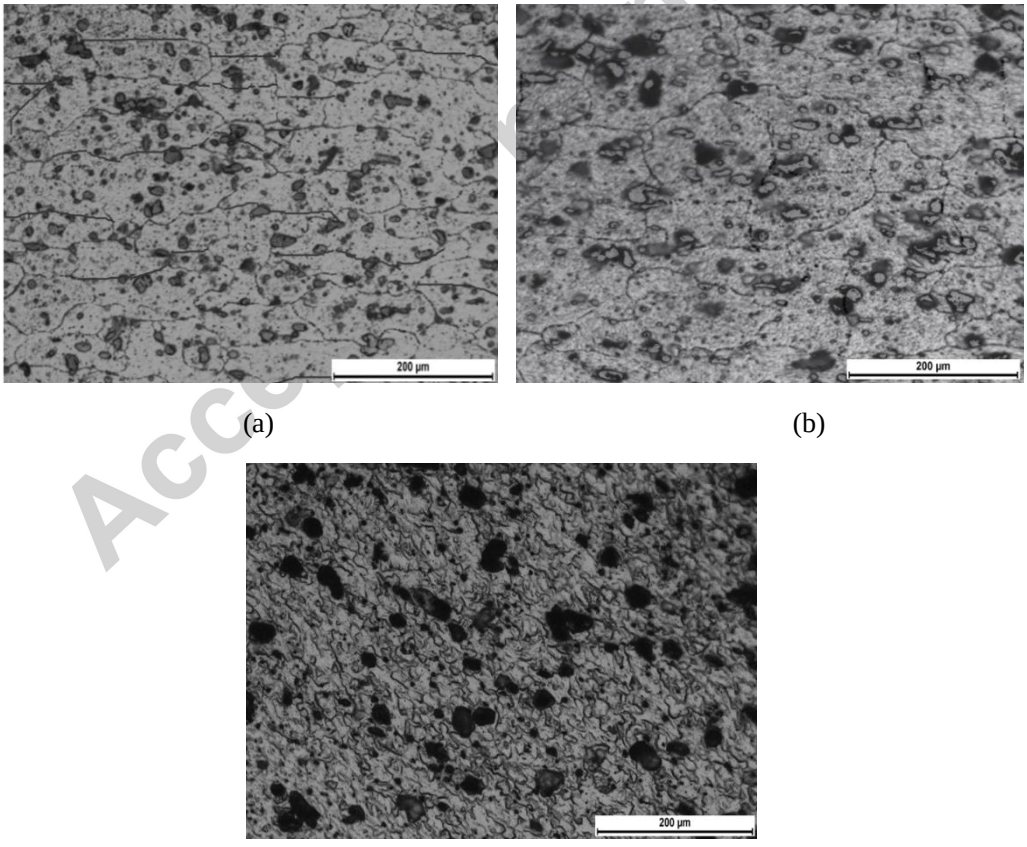

(a) (b)

(c)

Fig. 8. The microstructures of the 2219 AAWP: (a) parent metal; (b) HAZ; (c) weld bead.

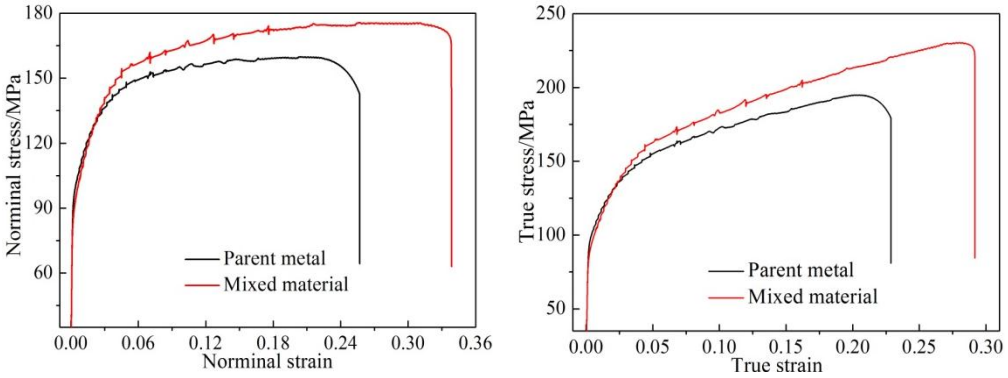

(a) (b)

Fig. 9. The nominal stress-strain (a) and true stress-strain (b) curves of the parent metal and mixed material of the 2219 AAWP.

3.1.1.4. Determination of continuous constitutive model of the 2219 AAWP

According to the method for establishing the continuous constitutive model of welded plate proposed in section 2, the continuous constitutive model of the 2219 AAWP was obtained, as shown in Eq. (25).

$$\begin{cases} \sigma_{hla} = 255.051(\varepsilon+0.000258)^{0.170} + \\ \quad \left[1112.693(\varepsilon+0.00196)^{0.204} - 956.441(\varepsilon+0.000258)^{0.170}\right]e^{0.53x}, & -7.00mm \le x \le -2.50mm \\ \sigma_{w} = 1112.693(\varepsilon+0.00196)^{0.204} - \\ \quad 701.387(\varepsilon+0.000258)^{0.170}, & -2.50mm \le x \le 0.50mm, -4.50mm \le x \le -3.00mm \\ \sigma_{hlr} = 255.051(\varepsilon+0.000258)^{0.170} + \\ \quad \left[513.322(\varepsilon+0.00196)^{0.204} - 441.238(\varepsilon+0.000258)^{0.170}\right]\frac{1}{1+10^{0.25x-1.33}}, & 0.50mm \le x \le 6.00mm \\ \sigma_{hua} = 255.051(\varepsilon+0.000258)^{0.170} + \\ \quad \left[1112.693(\varepsilon+0.00196)^{0.204} - 956.441(\varepsilon+0.000258)^{0.170}\right]e^{0.59x}, & -8.00mm \le x \le -4.50mm. \\ \sigma_{hur} = 255.051(\varepsilon+0.000258)^{0.170} + \\ \quad \left[1112.693(\varepsilon+0.00196)^{0.204} - 956.441(\varepsilon+0.000258)^{0.170}\right]e^{-0.39x}, & -3.00mm \le x \le 8.00mm \end{cases} \quad (25)$$

According to Eq. (25), the distributions of the flow stress-strain along the distance to the center of the weld were obtained, as shown in Fig. 10. As can be seen from the Fig. 10(a), in the lower zone, the flow stress of the weld bead is largest, and the flow stress declines gradually from the weld bead to the parent metal. The variation trend of flow stress in the upper zone (Fig. 10(b)) is similar to that in the lower zone (Fig. 10(a)).

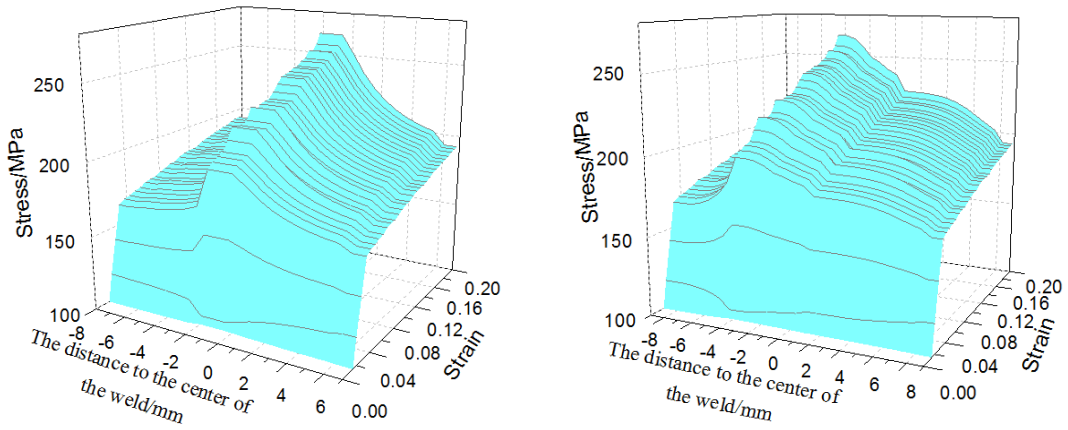

(a) (b)

Fig. 10. The distributions of the flow stress-strain along the distance to the center of the weld: (a) in the lower zone; (b) in the upper zone.

3.1.2. The continuous constitutive model of the QSTE340 WT

The geometric parameters of the QSTE340 WT used in this study are shown in Table 1, which are the same as those in the study of Ren et al. [25]. The relationships between true stress and strain of parent metal and mixed material are shown in Fig. 11 [25]. As seen from the figure, the mechanical properties of the mixed material have a great difference with the parent metal. The yield stress of the mixed material is higher than that of the parent metal, while its elongation is obviously smaller. The true stress-strain curves of parent metal and mixed material specimens of the QSTE340 WT were fitted by Eq. (22) [24], respectively, and the fitting results are shown in Eqs. (26) and (27), with the fitting precisions R of 0.95 and 0.96, respectively.

$$\sigma_p = 764.663(\varepsilon + 0.1640)^{0.266} \tag{26}$$

$$\sigma_m = 619.402(\varepsilon + 0.0108)^{0.048} \tag{27}$$

Table 1 The geometric parameters of the QSTE340 WT [25].

Parameters	Values
Tube specifications (D×T× L) /mm	Ø 60×4×90
Width of weld bead /mm	0.40
Width of HAZ /mm	13
Width of mixed material specimen /mm	15
Thickness of mixed material specimen /mm	4

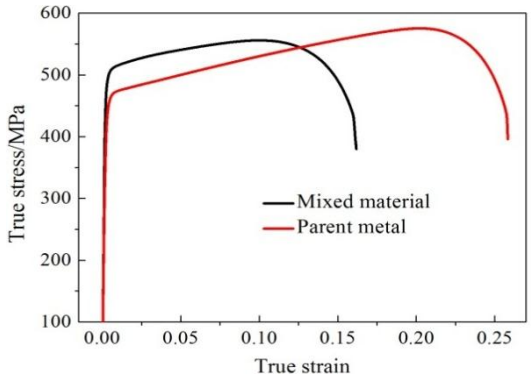

Fig.11. The true stress-strain curves of parent metal and mixed material of the QSTE340 WT [25].

3.1.2.1. Determination of microhardness variation

Since the microhardness of both sides of the weld bead in the QSTE340 WT is symmetrically distributed [25], a half-tube is adopted in this study. The microhardness distribution on the half-tube is shown in Fig. 12. As seen from the figure, the microhardness declines gradually from the weld bead to the parent metal. The trend of variation can be described by the exponential decay function (Eq. (7)). Therefore, fitting the relationship of microhardness with central angle by the function, Eq. (28) was obtained, with the fitting precision R of 0.95.

$$HV_{\mathrm{h}} = 167.87 + 45.76\mathrm{e}^{-8.88\alpha} \tag{28}$$

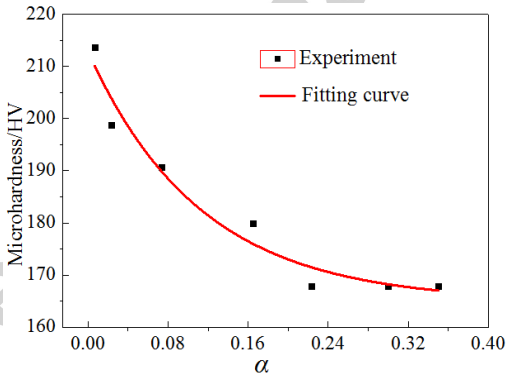

Fig. 12. The microhardness distribution and fitting curve of the QSTE340 WT.

3.1.2.2. Determination of continuous constitutive model of the QSTE340 WT

According to the proposed method for establishing the continuous constitutive model of welded tube in section 2, the continuous constitutive model of the QSTE340 WT was obtained, as shown in Eq. (29).

$$\begin{cases} \sigma_w = 1604.251(\varepsilon+0.011)^{0.048} - 1208.168(\varepsilon+0.164)^{0.266}, & 0 \le \alpha \le 0.0067 \\ \sigma_h = 764.663(\varepsilon+0.164)^{0.266} + \\ \quad \left[1604.251(\varepsilon+0.011)^{0.048} - 1972.831(\varepsilon+0.164)^{0.266}\right]e^{-8.88\alpha}, & 0.0067 \le \alpha \le 0.2230 \end{cases} \tag{29}$$

According to Eq. (29), the distributions of the flow stress-strain along the center

angle of the QSTW340 WT were obtained, as shown in Fig. 13. As seen from Fig. 13, at the same strain, the stresses in the weld bead are the largest, and the stresses in HAZ decline gradually from the weld bead to the parent metal.

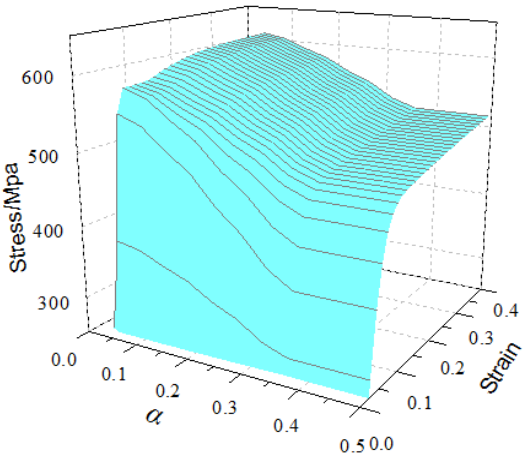

Fig. 13. The distributions of the flow stress-strain along the central angle of the QSTE340 WT.

3.2. Evaluation of the continuous constitutive models

3.2.1. Evaluation by applying to uniaxial tension tests of 2219 AAWP

To evaluate the accuracy of the continuous constitutive model of the 2219 AAWP, this constitutive model was applied to the FE modelings of longitudinal and transverse tensions of 2219 AAWP. The accuracy was verified by comparing the simulation with the experiment results in load-displacement curve of longitudinal tension and the maximum principal strain distribution of transverse tension.

Fig. 14 shows the curves of load versus extension of gauge length from simulation and experiment during the longitudinal tension of 2219 AAWP. As seen from the figure, the simulated load-displacement curve agrees well with the experimental one. The average error of the simulation relative to the experiment is only 1.8%, which indicates that this continuous constitutive model can accurately describe the load-deformation response of the welded metals in longitudinal tension.

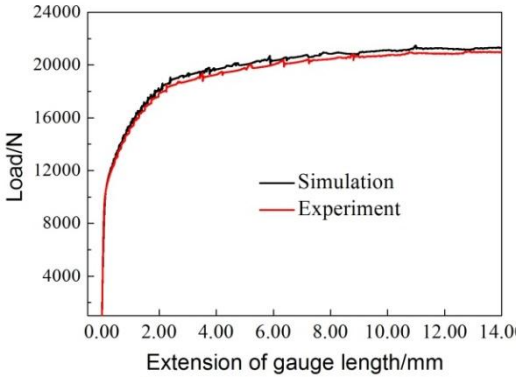

Fig. 14. Simulated and experimental load-displacement curves of 2219 AAWP in longitudinal tension.

Figs. 15 and 16 show the maximum principal strain distributions from simulation and experiment on the lower and upper surfaces of the specimen at different elongations (δ) during the transverse tension of 2219 AAWP. From the strain distributions on the lower surface in Fig. 15, the strains in the weld bead are the smallest, and they increase gradually from the weld bead to the parent metal. The maximum principal strain distributions on the lower surface from simulation and experiment agree well.

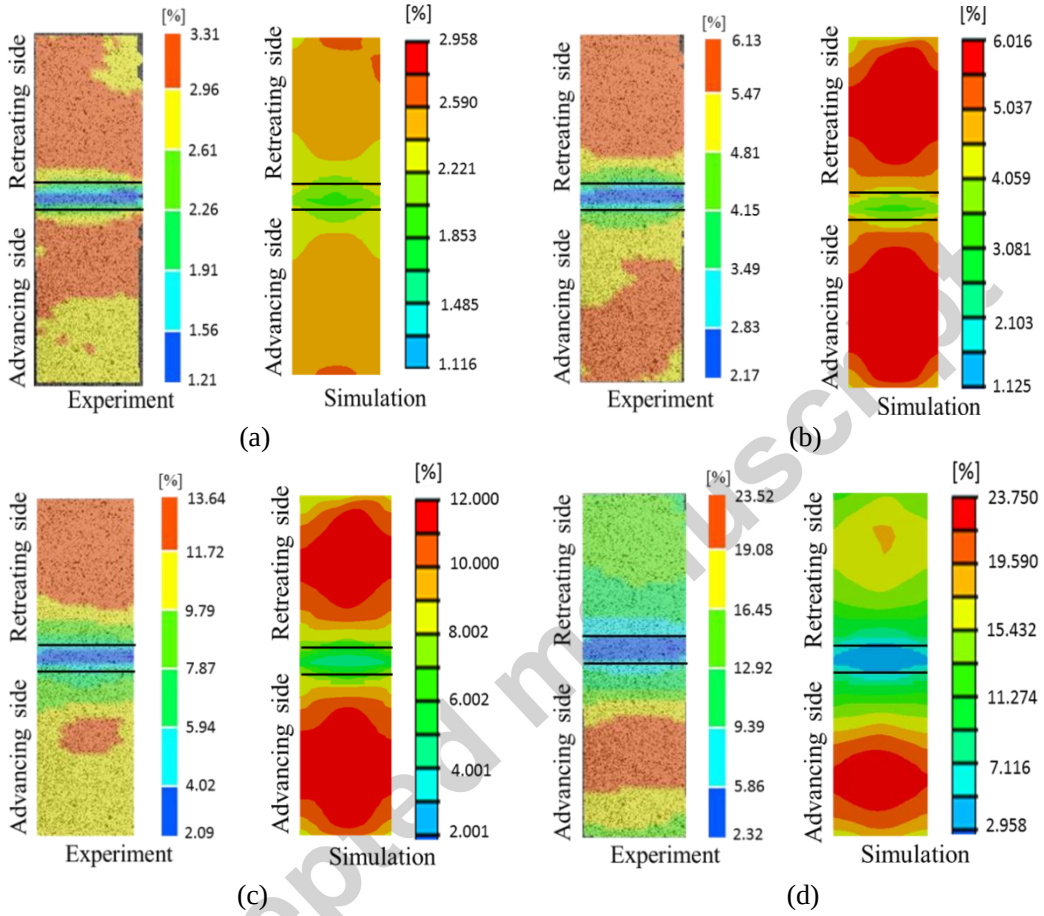

Fig. 15. The maximum principal strain distributions on the lower surface of the specimen at different δ in FE and experiment: (a) δ= 3.7%; (b) δ= 7.4%; (c) δ= 14.7%; (d) δ= 18.5%.

From the strain distributions on the upper surface in Fig. 16, in the late stage of the transverse tension (Figs.16(c) and (d)), the distribution and variation of the strain in simulation are consistent with those in the experiment, and the strains increase gradually from the weld bead to the parent metal. While in the initial stage (Figs. 16(a) and (b)), a large local strain occurred at the interface between the retreating side of the weld and the parent metal on the upper surface only in experiment.

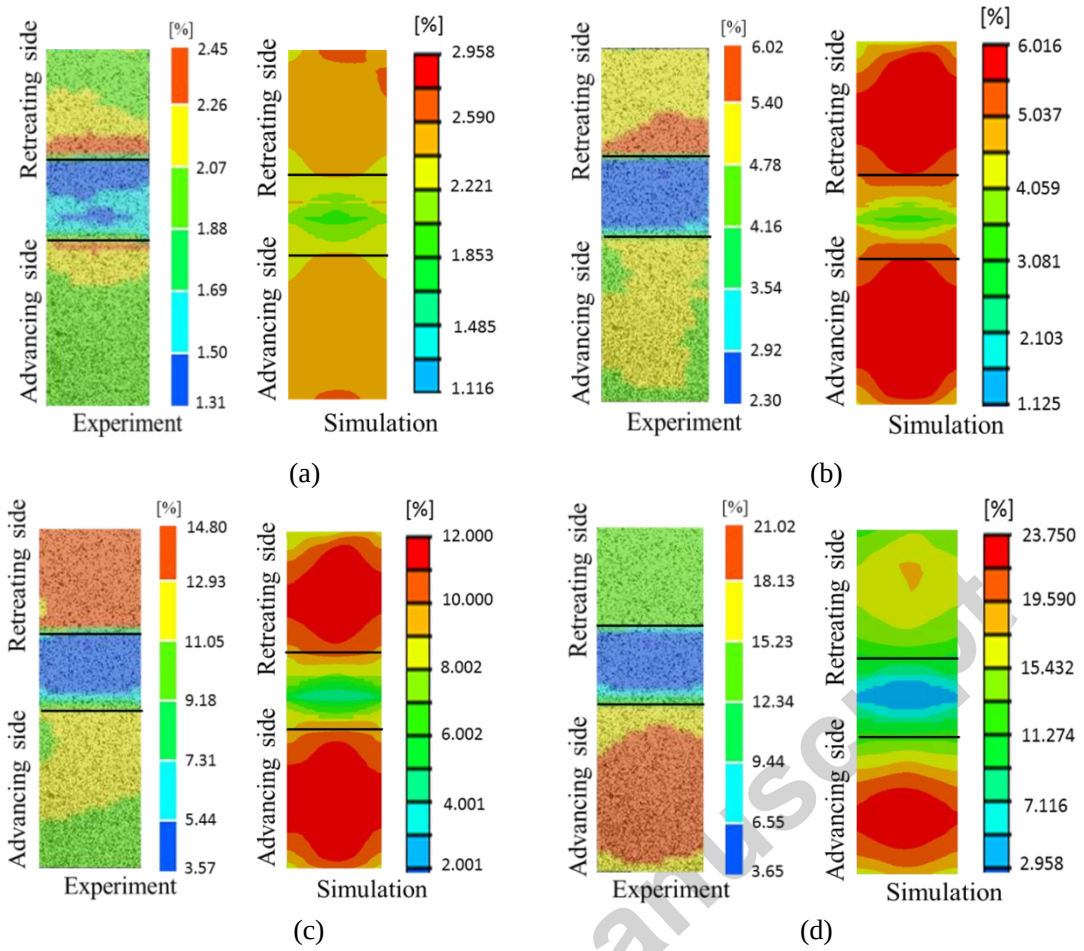

Fig. 16. The maximum principal strain distributions on the upper surface of the specimen at different δ in FE and experiment: (a) δ= 3.7%; (b) δ= 7.4%; (c) δ= 14.7%; (d) δ= 18.5%.

In order to intuitively observe the distributions of maximum principal strain, the distributions of the strain along the longitudinal centerline on the upper and lower surfaces in simulation and experiment were extracted, as shown in Fig. 17. As seen from Fig. 17, the strain values of simulation with the experiment agree well overall. When δ is 3.70%, 7.40% and 14.70%, the average errors of the simulation relative to the experiment in the weld are 11.13%, 16.43% and 17.88%, respectively, on the lower surface. They are 13.05%, 18.11% and 22.34% on the upper surface, respectively.

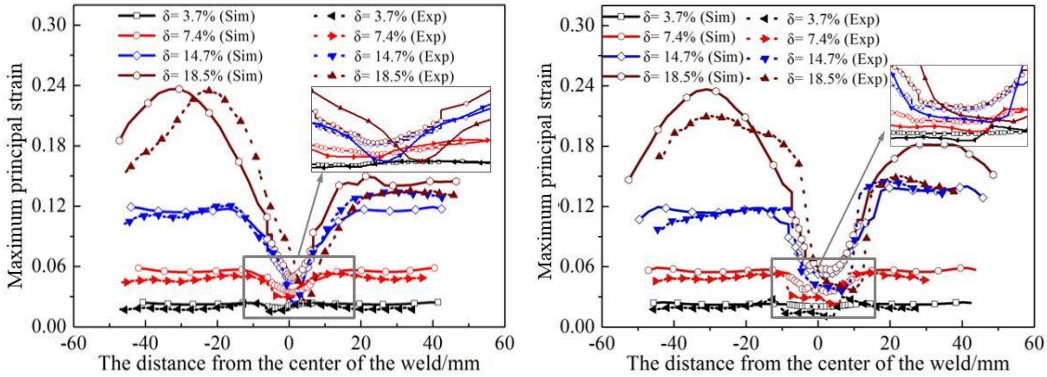

(a) (b)

Fig. 17. The maximum principal strain distributions along the longitudinal centerline (a) on the lower surface (b) on the upper surface in FE and experiment.

The possible reasons for above differences come from the error of the experimental instrument. Meanwhile, in the experiment, the material properties of welded joint unevenly distribute along the thickness direction. However, in the simulation, only the upper and lower two zones along the thickness direction, with uniform material properties in each zone, were applied. This simplification may also bring about some errors.

Through the above comparisons, it can be known that the continuous constitutive model of the 2219 AAWP established by the proposed method can accurately describe the deformation response of the welded metals in transverse tension.

Based on the simulation results presented above, the transverse tensile deformation behavior of the 2219 AAWP was obtained. As can be seen from Fig. 17, the strains in the weld are always lower than those of the parent metal, and the strains of the weld bead in the weld are the smallest. When δ is 3.70%, 7.40% and 14.70%, the strain differences between the weld bead and the parent metal are 0.021, 0.069 and 0.164 on the lower surface, respectively. They are 0.002, 0.019 and 0.060 on the upper surface, respectively. These differences and variations show that the maximum principal strain distributions along the axial and thick directions of the specimen are all uneven. Meanwhile, as the degree of deformation increases, these strain differences significantly increase. Moreover, the asymmetries of the strain distribution on the advancing and retreating sides become more and more obvious. The strain concentration is more likely to occur on the advancing side than the retreating side, which can be attributed to the higher temperature of the advancing side during welding process and the coarser grains. Hence the strength of the advancing side is relatively low, which makes it easier to appear the strain concentration.

3.2.2. Evaluation by applying to QSTE340 WT bending

To evaluate the accuracy of the continuous constitutive model of the QSTE340 WT, the constitutive model was applied to the FE modelings of welded tube bending. The accuracy was verified by comparing the predictions of the bending using the continuous and discrete constitutive models, respectively. The predictions include the thickness variation, the flattening rate of section and the springback angle. The thickness variation and the flattening rate of section were expressed by Eqs. (30) and (31), respectively.

$$\Delta t = (t' - t)/t \times 100\% \tag{30}$$

$$\Delta D = (D' - D)/D \times 100\% \tag{31}$$

where t and t' are the thickness of the tube before bending and after bending, respectively; D and D' are the diameter of the tube before bending and after bending,

respectively. The bending angle is 90° in this study, and the measuring positions are shown in Fig. 18.

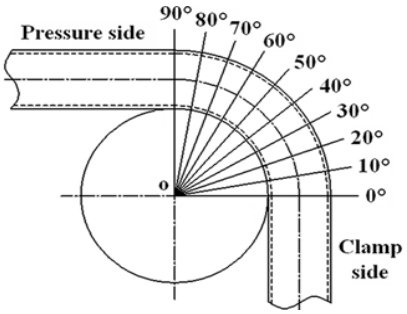

Fig. 18. The measuring positions.

Two bending processes with the weld on the inside and outside of the bend, respectively, were investigated in this study. The predicted results based on the continuous constitutive model and the discrete constitutive model (from Ren et al. [25]) and the experimental results are obtained, as shown in Figs. 19 to 22.

For the wall thinning degree, when the weld locates on the inside, as seen from Fig. 19(a), the trends of both kinds of predictions basically agree with the experimental results. Furthermore, the predictions of this study are closer to the experimental values at the start and end positions of bending. Fig. 19(b) illustrates that the differences between this study and experiment are smaller. The average errors of the wall thinning degree of Ren et al. [25] and this study are 33.42% and 13.70%, respectively, as compared with the experimental results. When the weld locates on the outside, from Fig. 20 (a), it can be clearly seen that the prediction results of this study are closer to the experimental results, even basically equal at the start position of bending. As seen from Fig. 20 (b), the differences of the wall thinning degree between this study and experiment are smaller, as the average errors of Ren et al. [25] and this study are 28.99% and 6.13%, respectively.

For the cross-sectional deformation degree when the weld locates on the inside (Fig. 21 (a)), the predicted error in this study was decreased by 6.69% compared with the Ren et al.'s [25]. When the weld locates on the outside (Fig. 21 (b)), the results of this study locate between the experimental and Ren et al.'s [25] results, presenting high prediction precision. The predicted error was decreased by 4.61% relative to the Ren et al.'s [25].

About the springback angle, Ren et al. [25] found that the weld on the inside and outside of the bend has little effect on the springback angle during the bending of the welded tube. Therefore, this study only compared the springback angles between FE and experiment when the weld locates on the inside, as shown in Fig. 22. This figure shows that the result of this study is closer to the experimental value. The average error of this study decreases by 4.30% compared with Ren et al.'s [25].

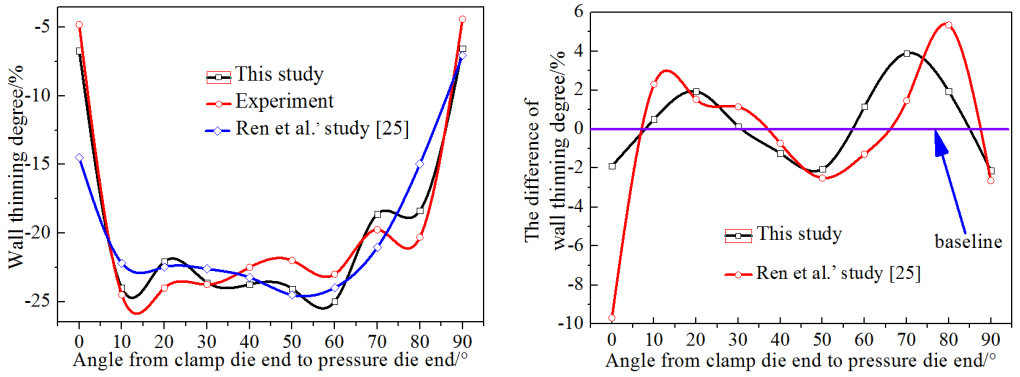

(a) (b)

Fig.19. The wall thinning degrees from FE and experiment (a) and the difference between simulation and experiment (b) when the weld locates on the inside of the bend.

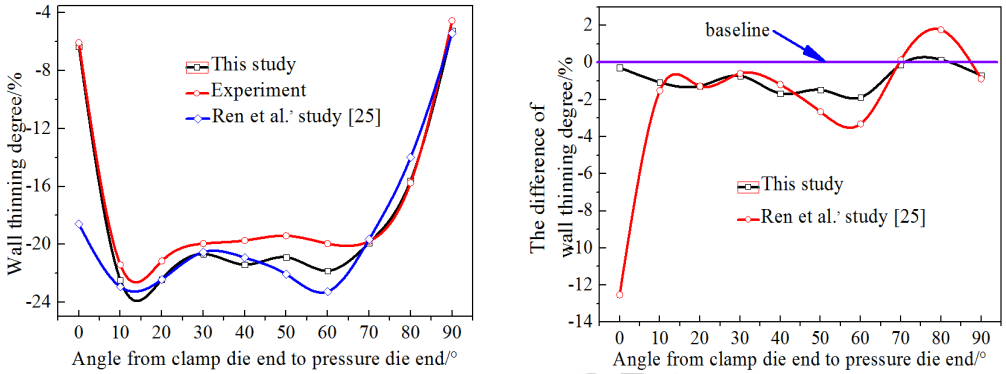

(a) (b)

Fig. 20. The wall thinning degrees from FE and experiment (a) and the difference between simulation and experiment (b) when the weld locates on the outside of the bend.

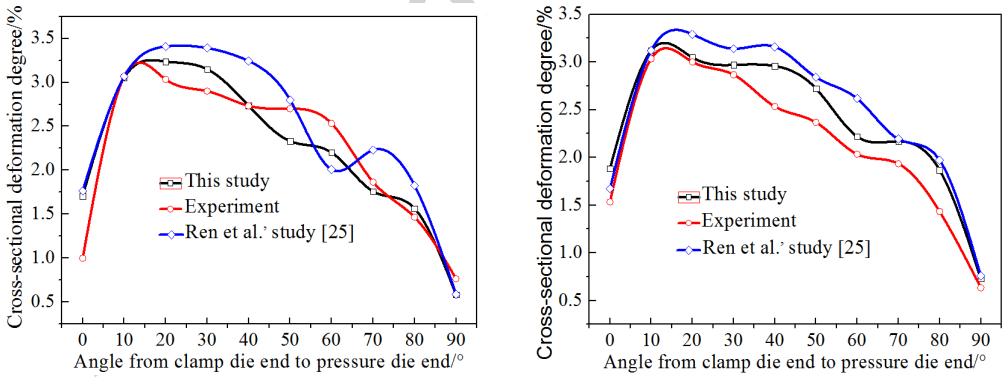

(a) (b)

Fig.21. The cross-sectional deformation degrees from FE and experiment when the weld locates on the inside (a) and outside (b) of the bend.

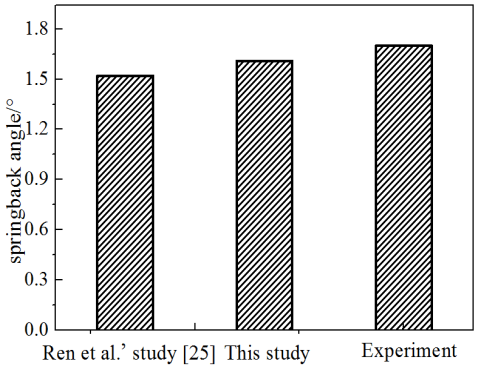

Fig.22. The springback angles from FE and experiment when the weld locates on the inside of the bend.

The above comparisons in the wall thinning degree, the cross-sectional deformation degree and the springback angle show that the continuous constitutive model of the QSTE340 WT can accurately predict the plastic deformation behavior and present higher prediction accuracy in the complicated plastic forming process.

4. Conclusions

(1) A universal method was proposed for establishing continuous constitutive models of welded metals. In this method, the continuous variation in flow stress across the weld bead and HAZ was established by using the microhardness as a bridge between the flow stress and the weld shape. Through the method, the constitutive model of the welded metal can be expressed as a function of weld shape.

(2) Using the proposed method, the continuous constitutive models of a 2219 AAWP and a QSTE340 WT were set up. These constitutive models were evaluated by applying to the longitudinal and transverse tension tests of the 2219 AAWP and the bending of the QSTE340 WT. The comparisons among the simulation and experiment show that the continuous constitutive models can accurately describe the deformation responses of the welded metals in the simple and complicated plastic deformation processes and present higher prediction accuracy.

(3) During the transverse tension of the 2219 AAWP, the maximum principal strain in the weld is always lower than that of the parent metal. As the degree of deformation increases, the strain difference increases. Meanwhile, the strain concentration is more likely to occur on the advancing side.

Acknowledgements

The authors acknowledge support from the National Science Fund for Distinguished Young Scholars of China (51625505) and the Key Program Project of the Joint Fund of Astronomy and National Science Foundation of China (Project U1537203).

References

[1] M.S.J. Hashmi, Aspects of tube and pipe manufacturing processes: Meter to nanometer diameter, J. Mater. Proc. Technol. 179(2006) 5-10.

[2] Z. Mei, K. Guo, H. Yang, Advances and trends in plastic forming technologies for welded tubes, Chinese J Aeronaut. 29(2016) 305-315.

[3] S.K. Panda, D.R. Kumar, Improvement in formability of tailor welded blanks by application of counter pressure in biaxial stretch forming, J. Mater. Proc. Technol. 204(2008) 70-79.

[4] M. Kleiner, M. Geiger, A. Klaus, Manufacturing of Lightweight Components by Metal Forming, CIRP Ann. Manuf. Technol. 52(2003) 521-542.

[5] K.M. Zhao, B.K. Chun, J.K. Lee, Finite element analysis of tailor-welded blanks, Finite Elem. Anal. Des. 37(2001) 117-130.

[6] B.Y. Ghoo, Y.T. Keum, Y.S. Kim, Evaluation of the mechanical properties of welded metal in tailored steel sheet welded by CO_2 laser, J. Mater. Proc. Technol. 113(2001) 692-698.

[7] S.K. Panda, D.R. Kumar, H. Kumar, A.K. Nath, Characterization of tensile properties of tailor welded IF steel sheets and their formability in stretch forming, J. Mater. Proc. Technol. 183(2007) 321-332.

[8] A.A. Zadpoor, J. Sinke, R. Benedictus, R. Pieters, Mechanical properties and microstructure of friction stir welded tailor-made blanks, Mater. Sci. Eng. A 494(2008) 281-290.

[9] C.H. Cheng, M. Jie, L.C. Chan, C.L. Chow, True stress–strain analysis on weldment of heterogeneous tailor-welded blanks—a novel approach for forming simulation, Int. J. Mech. Sci. 49(2007) 217-229.

[10] F.I. Saunders, R.H. Wagoner, Forming of tailor-welded blanks, Metall. Mater. Trans. A 27(1996) 2605-2616.

[11] K. Abdullah, P.M. Wild, J.J. Jeswiet, A. Ghasempoor, Tensile testing for weld deformation properties in similar gage tailor welded blanks using the rule of mixtures, J. Mater. Proc. Technol. 112(2001) 91-97.

[12] W. Lee, K.H. Chung, D. Kim, J. Kim, C. Kim, K. Okamoto, R.H. Wagoner, K. Chung, Experimental and numerical study on formability of friction stir welded TWB sheets based on hemispherical dome stretch tests, Int. J. Plasticity 25(2009) 1626-1654.

[13] A. Reis, P. Teixeira, J. Ferreira Duarte, A. Santos, A. Barata Da Rocha, A.A. Fernandes, Tailored welded blanks–an experimental and numerical study in sheet metal forming on the effect of welding, Comput. Struct. 82(2004) 1435-1442.

[14] A.P. Roque, R.M. Natal Jorge, M.P.L. Parente, A.R. Fontes Valente, A. Antonio Fernandes, in: E. Onate, D.R.J. Owen (Eds.), Proceedings of the VIII International~Conference on Computational Plasticity, Barcelone, Spain, CIMNE, 2005, pp.1–4.

[15] G. Li, F. Xu, G. Sun, Q. Li, Identification of mechanical properties of the weld line by combining 3D digital image correlation with inverse modeling procedure, Int. J. Adv. Manuf. Technol. 74(2014) 893-905.

[16] M. Zhan, H. Du, J. Liu, N. Ren, H. Yang, H. Jiang, K. Diao, X. Chen, A method for establishing the plastic constitutive relationship of the weld bead and heat-affected zone of welded tubes based on the rule of mixtures and a microhardness test, Mater. Sci. Eng. A 527(2010) 2864-2874.

[17] S.D. Raymond, P.M. Wild, C.J. Bayley, On modeling of the weld line in finite element analyses of tailor-welded blank forming operations, J. Mater. Proc. Technol. 147(2004) 28-37.

[18] K. Chung, W. Lee, D. Kim, J. Kim, K.H. Chung, C. Kim, K. Okamoto, R.H. Wagoner, Macro-performance evaluation of friction stir welded automotive tailor-welded blank sheets: Part I− Material properties, Int. J. Solids Struct. 47(2010) 1048-1062.

[19] D. Kim, W. Lee, J. Kim, C. Kim, K. Chung, Formability evaluation of friction stir welded 6111-T4 sheet with respect to joining material direction, Int. J. Mech. Sci. 52(2010) 612-625.

[20] Y. Song, L. Hua, D. Chu, J. Lan, Characterization of the inhomogeneous constitutive properties of laser welding beams by the micro-Vickers hardness test and the rule of mixture, Mater. Des. 37(2012) 19-27.

[21] Y.L. Song, L. Hua, F.Z. Meng, Inhomogeneous constructive modelling of laser welded bead based on nanoindentation test, Ironmak Steelmak 39(2012) 95-103.

[22] A.N. Li Jun, Z.J. Zhang, Discussion on the vickers hardness test within the HAZ of weld joints, Physical Testing & Chemical Analysis Parta Physical Testing (2002).

[23] Zhao Y, Plastic Formability of 2219 Aluminum Alloy Friction Stir Welded Sheet, Harbin Institute of Technology (2015).

[24] H. J. Swift, Plastic instability under plane stress, J. Mech. Phys. Solids. 1(1952) 1-18.

[25] R. Ning, Study on Deformation Compatibility and Bending Limit in Steel Welded Tube NC Bending Processes, Northwestern Polytechnical University (2013).